Spring 4-26-2022

Collision-Induced Dissociation and Ion Mobility Mass Spectrometry of Au30(S-tBu)18 Nanoclusters

Christopher Hood

COLLISION-INDUCED DISSOCIATION AND ION MOBILITY MASS SPECTROMETRY OF $Au_{30}(S\text{-}t\text{Bu})_{18}$ NANOCLUSTERS

By

Christopher Harrison Hood

A thesis submitted to the faculty of The University of Mississippi in partial fulfillment of the requirements of the Sally McDonnell Barksdale Honors College.

Oxford, MS

May 2022

Approved By

_____

Advisor: Professor Amala Dass

_____

Reader: Professor Saumen Chakraborty

_____

Reader: Professor Daniell Mattern

ACKNOWLEDGEMENTS

This work is dedicated to my family, friends, and professors. I thank the Sally McDonnell Barksdale Honors College for encouraging me and providing an avenue to complete my thesis project. I thank my research advisor, Dr. Amala Dass, for providing insights and wisdom to the research process. A special thanks to my grandfather, Dr. Lester Harrison, for reading and discussing my thesis work as well as for inciting my love for chemistry. I thank my readers, Dr. Saumen Chakraborty and Daniell Mattern, for their support and help with revisions. Lastly, I thank Hirunika Wijesinghe, Senthil Eswaramoorthy, and Naga Arjun Sakthivel for teaching me valuable skills throughout my time in the lab and for always being there when I needed help.

ABSTRACT

Collision Induced Dissociation (CID) and Ion Mobility Mass Spectrometry (IM-MS) are methods used to understand the structural arrangement and stability of large molecules. In this study, the gold nanocluster $Au_{30}(S\text{-}t\text{Bu})_{18}$ was dissociated at varying Trap collision energies, and drift time vs mass spectrometry data was plotted to determine the order of cluster fragmentation. Comparing $Au_{30}(S\text{-}t\text{Bu})_{18}$ data to that of $Au_{25}(SCH_2CH_2Ph)_{18}$, the only current nanocluster published with IM-MS data, two distinctly different dissociation patterns were seen. Unlike the linear CID fragmentation of $Au_{25}(SCH_2CH_2Ph)_{18}$ from the parent ion to the resulting Au_{13} core, $Au_{30}(S\text{-}t\text{Bu})_{18}$ fragments into two species regions: $Au_{30}(X)_{11\text{-}18}$ and $Au_{26}(X)_{9\text{-}14}$, where x is the total number of ligands, S and S-*t*Bu. These two regions remained present in ionization even at the highest Trap collision energy (200 V). The presence of the two $Au_{30}(S\text{-}t\text{Bu})_{18}$ species regions can be seen in both CID mass spec and IM-MS drift time bands. IM-MS m/z vs drift time plots of $Au_{30}(S\text{-}t\text{Bu})_{18}$ show two broad positively sloped fragment bands with no viewable fragmentation below $Au_{26}S_9$. Identification of $Au_{30}(S\text{-}t\text{Bu})_{18}$ fragment peaks shows a systematic loss of -S-*t*Bu, -*t*Bu, and -S groups in the protecting thiolate ligand monolayer to the gold core with minimal to no loss of Au atoms. The ability of $Au_{30}(S\text{-}t\text{Bu})_{18}$ to lose almost all the protecting carbon chains without loss of Au from the core may be a result of the stability of the Au core structure. Additionally, the high loss of *tert*-butyl groups in $Au_{30}(S\text{-}t\text{Bu})_{18}$ collision, unseen in $Au_{25}(SCH_2CH_2Ph)_{18}$, may be due to the inherent stability of the tertiary carbocation of *tert*-butyl after cleavage from the S atom.

TABLE OF CONTENTS

LIST OF FIGURES

LIST OF TABLES

LIST OF ABBREVIATIONS

AuNCs – Gold Nanoclusters

CID – Collision-Induced Dissociation

DCTB - Trans-2-[3-(4-*tert*-butylphenyl)-2-methyl-2-propenylidene]malononitrile

ESI-MS – Electrospray Ionization Mass Spectroscopy

ESI-MS/MS – Electrospray Ionization Tandem Mass Spectroscopy

THF – Tetrahydrofuran

IM-MS – Ion Mobility Mass Spectrometry

MALDI-TOF – Matrix-Assisted Laser Desorption Ionization Time-of-Flight

SEC – Size Exclusion Chromatography

SR- Thiol

TOF – Time-of-Flight

PC2 – Phenylethanethiol

PDT – Photodynamic Therapy

PTT – Photothermal Therapy

UV-vis – Ultraviolet-Visible Absorption Spectroscopy

XRD – X-ray Diffraction

Chapter 1

Introduction to Gold Nanoclusters, Synthesis of $Au_{30}(S\text{-}tBu)_{18}$, and Crystal Structures

1.1 Gold Nanoclusters

Gold-thiolate clusters, or gold nanoclusters, are compounds of nanometer size consisting of a fixed number of gold atoms surrounded and stabilized by thiolate ligands[1]. Specifically, gold nanoclusters (AuNCs) represent gold-thiolate compounds that are less than three nanometers (<3 nm) in size[2]. While the terms nanoclusters and nanoparticles are sometimes used interchangeably, this paper will define nanoclusters as compounds less than 3 nm in size and nanoparticles as compounds greater than 3 nm is size. The common notation for gold nanoclusters is $Au_n(SR)_m$, with *n* representing the number of gold atoms and *m* representing the number of thiolate ligands[1,3,4].

The structure of AuNCs consists of three main parts: an inner gold core, an Au-thiol staple motif, and an outer thiolate layer[1,3,5]. The inner gold core consists entirely of Au atoms arranged in stable geometric structures. Au-thiol staple motifs are the outer layer of Au atoms branching off the gold core. Staple motifs have alternating sequences of Au and thiol (SR) components that surround and protect the core. The types and abundance of staple motifs is highly influential on the final structure of AuNCs. Common staple motifs include bridging units (Au-SR), monomeric staples (SR-Au-SR), dimeric staples (SR-Au-SR-Au-SR), and trimeric staples (SR-Au-SR-Au-SR-Au-SR). Staple motifs such as bridging units, monomeric staples, and trimeric staples can be seen in the AuNC $Au_{30}(S\text{-}t\text{Bu})_{18}$[1,3]. Dimeric staples can be seen in the AuNC $Au_{25}(SCH_2CH_2Ph)_{18}$[5]. The use of staple motifs in the previously mentioned AuNCs will be discussed in future chapters.

1.2 Classes of Thiolate Ligands

Though all gold-thiolate clusters share a general structure of a gold core surrounded by a protective monolayer of thiolate ligands, the types of thiolate ligands used can vary wildly among compounds. Generally, there are three main classes of thiolate ligands: aliphatic, aromatic, and

bulky[6]. The class of thiolate ligand used has been found to greatly influence the structure of the gold core[7]. Aliphatic ligands are ligands containing a chain of organic carbon and hydrogen atoms in a non-aromatic structure[6]. For classification purposes in AuNCs, aliphatic ligands cannot be bulky in shape. Examples of a aliphatic ligands include phenylethanethiol (PC2), *n*-butanethiol, and dodecanethiol. Bulky ligands, though a type of aliphatic ligand, are going to be defined as any aliphatic thiolate ligand that demonstrates a branched, sterically hindered structure[6]. Examples of bulky ligands include *tert*-butylthiol and 1-adamantanethiol. Lastly, aromatic ligands are ligands containing a conjugated ring system of delocalized π bonds in connection with the thiol group[6]. Examples of a aromatic ligands include 4-*tert*-butylbenzenethiol and thiophenol. It is important that the aromatic ring be in direct contact with the sulfur of the thiol group in order for the AuNC to obtain the resonance benefits. For context, though phenylethanethiol and 4-*tert*-butylbenzenethiol both contain an aromatic ring, the phenylethanethiol ligand does not have an aromatic ring directly bound to the S atom of the thiol and therefore cannot be considered an aromatic ligand.

1.3: Applications of gold nanoclusters

Recent developments in gold nanocluster and nanoparticle research have shown promising benefits in the medical field. Using the physical and chemical properties of AuNCs, researchers can use nanomaterials for a wide range of medical applications. These desired AuNC properties include high X-ray absorption coefficients, easy synthetic manipulation, high surface binding affinity, low toxicity, and unique optical and electronic properties[8]. With these properties readily available in AuNCs, these materials can be used for activities such as photodynamic therapy, photothermal therapy, X-ray imaging, drug delivery, and sensing to name a few[8]. These applications will now be briefly explained.

Photodynamic therapy (PDT) is a form of light therapy that uses a photosensitizing substance to create free radicals in targeted areas to promote cell apoptosis[8]. Using the low toxicity and high light absorption of AuNCs, AuNCs can be injected into tumor sites and used as a photosensitizing substance to donate electrons that create free radicals for treatment of various oncological diseases[8]. Photothermal therapy (PTT), or thermal ablation, is a minimally invasive cancer treatment involving the use of electromagnetic radiation in the form of heat to kill cancer cells[8]. With a high absorption near the infrared region, AuNCs can easily be heated under electromagnetic radiation inside the cancer tissue to kill malignant tumors[8]. In X-ray imaging of vascular vesicles, contrasting agents are injected into the bloodstream to highlight blood pathways under X-ray light[8]. These contrasting agents can be harmful to the body and have short retention times in the bloodstream. To address this concern, the high X-ray absorption coefficient and low toxicity properties of AuNCs can be used for safer imaging of the patient. Additionally, the large nature of AuNCs increase the retention time in the bloodstream, which in turn decreases the amount of contrasting agent needed[8]. Drug delivery involves the specific targeting and transportation of drugs to their intended location in the body[8]. Using the high surface area and ligand monolayer adjustability, AuNCs can bind specific proteins and RNA molecules to the outer monolayer and transport substances throughout the body[8]. Lastly, sensing is a broad term encompassing any use of a detector to detect ions or macromolecules in the body[8]. Applying the colorimetric, florescent, and electrical properties of AuNCs, specific macromolecules can be identified and quantified in the body[8].

1.4: Synthesis of $Au_{30}(S\text{-}tBu)_{18}$

1.4.1: Chemicals

Synthesis of $Au_{30}(S\text{-}tBu)_{18}$ requires the following: $HAuCl_4.3H_2O$, tertiary butylthiol (HS-*t*Bu), sodium borohydride ($NaBH_4$), HPLC grade tetrahydrofuran (THF), Toluene, Methanol, trans-2-[3-(4-*tert*-butylphenyl)-2-methyl-2-propenylidene]malononitrile (DCTB), and cesium iodide (CsI)[1].

1.4.2: Instrumentation

To understand the sizes and composition of AuNCs produced during synthesis, Matrix-assisted laser desorption ionization time-of-flight mass spectroscopy (MALDI-TOF-MS), Ultraviolet-visible absorption spectroscopy (UV-vis), and Electrospray ionization mass spectroscopy (ESI-MS) were used. MALDI-TOF is a mass spectrometry instrument used to determine the mass over charge (m/z) of a sample[9,10]. This process works by mixing the AuNC sample with a matrix, commonly DCTB, and pipetting a small amount of the resulting mixture onto a sample plate. Since ionization is needed for the instrument to detect the sample, DCTB is used to promote ionization of the AuNCs[10–12]. DCTB contains a high number of hydrogens that can easily dissociate and bind to the sample molecule, creating a net positive charge[12]. To guarantee the sample has enough hydrogens available to ionize, the volume ratio of DCTB to sample should be 100 µL to 1 µL respectively. Once the sample has been loaded onto the sample plate, the plate is then inserted into the MALDI device, and a vacuum is created inside the chamber. Next, a laser with a set intensity is pointed at the sample plate and ionization of the sample occurs. As the sample is ionized, charged molecules begin traveling up the time-of-flight tube until they reach a

detector. The time it takes the charged molecules to reach the detector, or TOF, along with the charge of the ion determines the m/z value for the molecule[9,11,12].

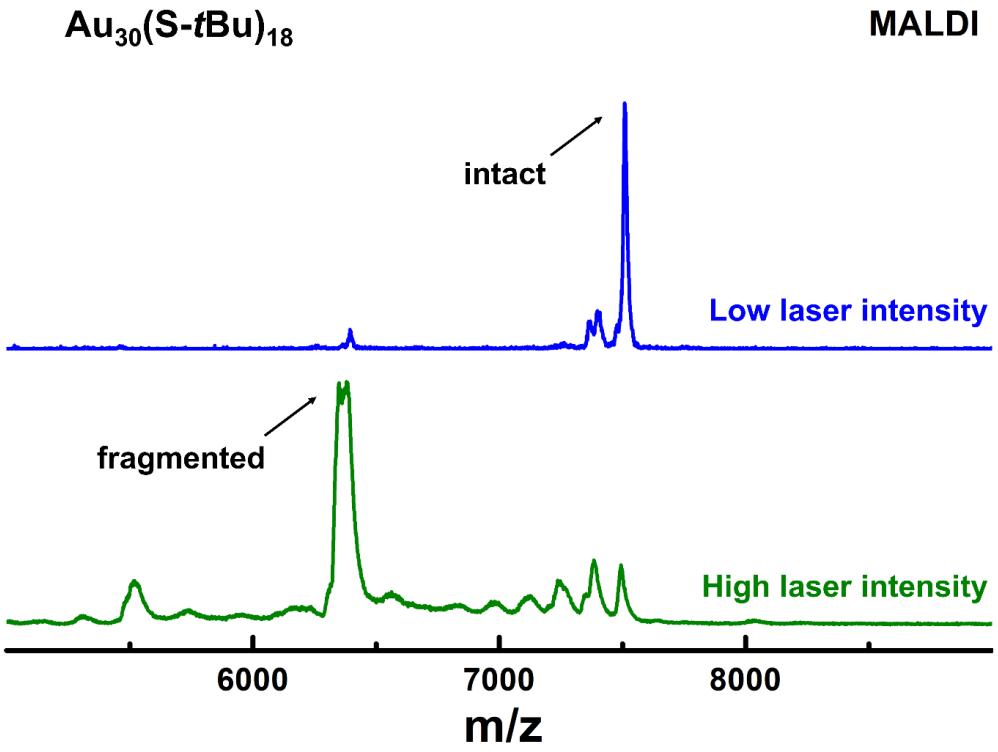

Figure 1.1: MALDI-MS data of $Au_{30}(S\text{-}t\text{Bu})_{18}$ demonstrating low laser intensity (blue) and high laser intensity (green) fragmentation. Low laser intensity reduces the amount of sample ionization but also lowers the degree of sample fragmentation (soft ionization). High laser intensity increases sample ionization but creates more fragmentation of the molecule (hard ionization).

While MALDI-TOF is a fast and effective way of identifying the relative mass sizes of the sample, it does not depict the compositional distribution of the various sizes or the isotopic distribution of peaks. Additionally, MALDI-TOF is known as a form of hard ionization for gold nanoclusters, since the intensity of the laser often fragments the sample during ionization[13]. As seen in Figure 1.1, the fragmentation of the sample can be lessened by reducing the intensity of

the laser, but some degree of fragmentation is difficult to avoid. As laser intensity is decreased, the amount of sample ionization also decreases and reduces the resolution of the mass spec data as well as the types of ions that can ionize. Therefore, MALDI-TOF is largely used for identifying the general presence of AuNC sizes.

To understand the purity and presence of AuNCs in solution, UV-visible spectroscopy methods were used. UV-visible spectroscopy is a device used to measure the UV light diffraction that molecules create when light is passed through a sample solution[14,15]. As UV light is projected through a clear sample cartridge containing a dissolved sample, some of the UV light becomes absorbed by the sample solution and does not make it through to the UV detector on the other side of the cartridge[14,15]. Comparing the amount of light emitted by the machine versus the amount of light detected by the sensor, a graph of UV absorption can be made across a given wavelength range. For AuNC purposes, the graph of UV absorption can show useful information about the relative purity of solution[14,15]. By comparing the absorption graph of a AuNC sample to that of a known pure sample, the degree of graph overlap can provide evidence to the sample purity. Additionally, key absorption bumps at particular wavelengths, or features, can be used to identify the AuNC sample. Figure 1.2 shows the difference in feature intensity between an etched sample of $Au_{30}(S\text{-}t\text{Bu})_{18}$ and a purer sample that has gone through SEC treatment. As $Au_{30}(S\text{-}t\text{Bu})_{18}$ becomes more concentrated in solution, the height of the feature at 600 nm grows. UV-visible spectroscopy was used alongside MALDI-MS to confirm the presence of $Au_{30}(S\text{-}t\text{Bu})_{18}$ during synthesis.

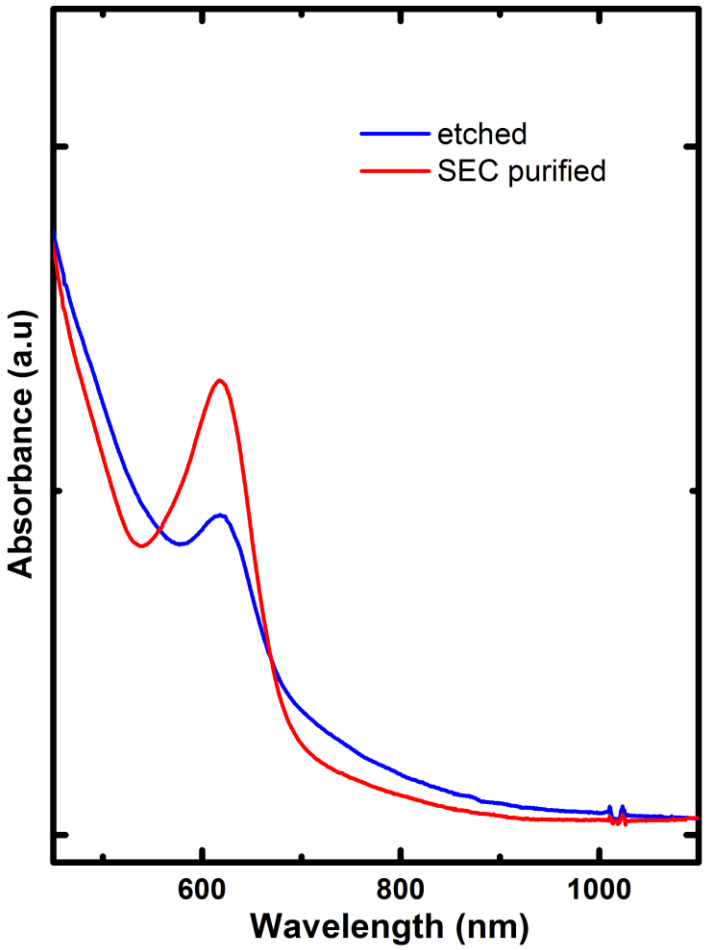

Figure 1.2: UV-vis absorption data of $Au_{30}(S\text{-}t\text{Bu})_{18}$ showing feature intensity in an etched sample (blue) and more purified SEC sample (red). $Au_{30}(S\text{-}t\text{Bu})_{18}$ has a prominent feature that can be seen at approximately 620 nm. The higher the feature height, the purer the $Au_{30}(S\text{-}t\text{Bu})_{18}$ sample is.

For compositional analysis and the precise identification of AuNC species, ESI-MS was used. ESI-MS is a method used to determine the precise m/z value of a sample molecule[1,16]. Similar to MALDI-MS, ESI-MS collects TOF data for ionized molecules injected into the instrument. However, ESI-MS distinguishes itself from MALDI-MS by its ability to determine the compositional distribution of ionized molecules and precisely measure the mass of a molecule

down to one Dalton. Unlike MALDI-MS, ESI-MS is a form of soft ionization[13]. Soft ionization, in contrast to hard ionization, is a form of ionizing that does not readily fragment the sample[13]. Soft ionization is often used when the exact mass of the sample is needed. Through the precision of ESI-MS, the isotopic distribution of a molecule can be viewed and used as an identifiable feature when assigning mass peaks[16]. ESI-MS will be further discussed with ESI-MS/MS in future chapters.

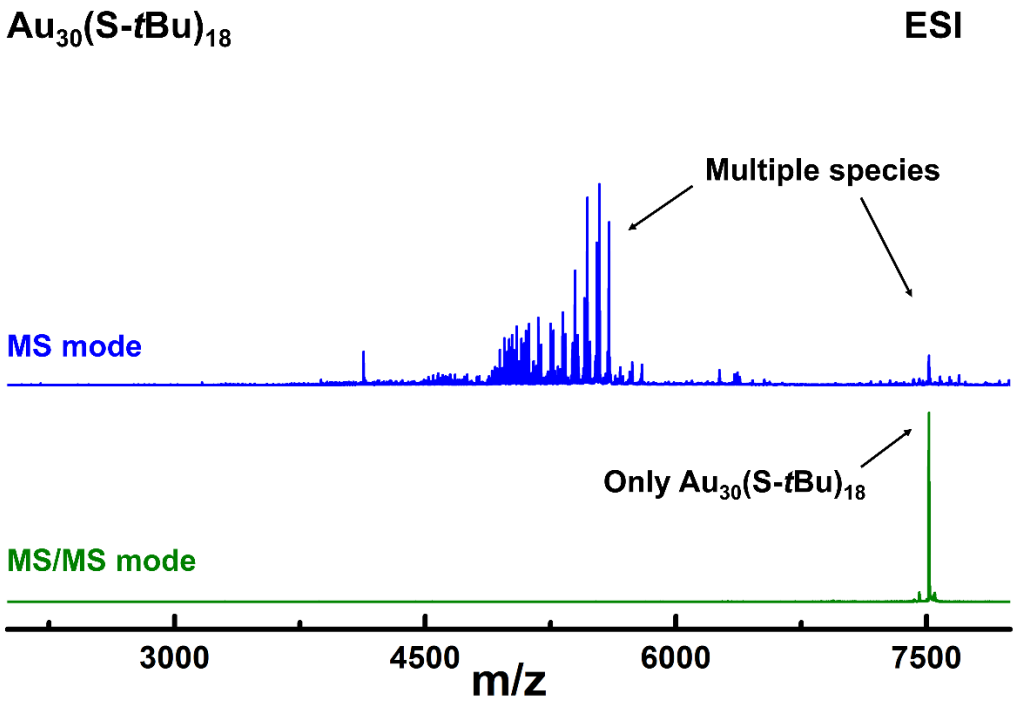

Figure 1.3: ESI data for an $Au_{30}(S\text{-}t\text{Bu})_{18}$ sample in MS (blue) and MS/MS (green) modes. The $Au_{30}(S\text{-}t\text{Bu})_{18}$ sample includes a mixture of AuNC sizes in the solution; however, the MS/MS mode allows for exclusive filtering of $Au_{30}(S\text{-}t\text{Bu})_{18}$ in the quadrupole of the ESI.

1.4.3: Crude Product

Synthesis of $Au_{30}(S\text{-}t\text{Bu})_{18}$ begins with the formation of a crude product in a one-phase synthesis. A crude product is a diverse solution of various AuNC sizes containing gold and

thiolate ligands[1,3]. The crude synthesis is one-phase since it is reacted in only one organic layer compared to the organic and aqueous layers of two-phase reactions[1]. To make the crude, 0.1 g of $HAuCl_4.3H_2O$ is dissolved in 15 mL of HPLC grade THF and reacted with 87 µL of HS-*t*Bu at a 1:3 molar ratio and stirred for 15 min at 450 rpm[1]. The molar ratio of gold hydrate to thiol is directly influential to the resulting size of AuNCs[6]. Next, 12 mmol of $NaBH_4$ dissolved in 10 mL of ice-cold water is added to the solution[1]. After $NaBH_4$ has been added, the solution is stirred for an additional hour and then washed three times with methanol and water[1]. Washing is a form of solvent cleaning in which a solution is mixed with hydrophilic solvents, such as water and methanol, until soluble impurities are dissolved into the hydrophilic solvent and centrifuged. After centrifuging, the hydrophilic solution is discarded, and the insoluble portion remains in the centrifuge tube. Since AuNCs are inherently hydrophobic, washing is a useful step in ridding the product solution of excess thiol and non-AuNC fragments.

1.4.4: Etching

The creation of a crude product creates a wide variety of AuNC sizes in solution[1]. To isolate a particular AuNC size, thermochemical treatment (commonly referred to as etching) is implemented. Etching is the process of placing a crude solution into a heated oil bath with excess thiol and allowing thermodynamic stability to eliminate unstable and unwanted AuNC species[1]. By setting the particular temperature of the oil bath, time in the bath, and molar ratio of thiol added, a specific AuNC species can be designated in solution. In the case of Au_{30}(S-*t*Bu)$_{18}$, the crude solution was mixed with 1 mL of Toluene and 1 mL of HS-*t*Bu and placed in a 70˚ C oil bath for 4 hours[1]. Following etching, the resulting product was washed three times with methanol and water.

1.4.5: Size Exclusion Chromatography (SEC)

Though thermochemical treatment is effective in eliminating many unstable species in the crude product, some stable sizes will still remain in addition to the target species. To purify the target species from the remaining etched solution, size exclusion chromatography (SEC) can be used. SEC is a process in which a solution is poured through a column of meshed beads, and particle sizes become separated based on size[16]. In this study, BioRed SX1 (styrene divinylbenzene) beads were used for all SEC separations[16]. As the solution travels down the column, large particles move around the beads and elute first, while smaller particles travel through the small pores of the beads and elute from the column later. By collecting elution samples from the column in different time intervals, specific particle sizes can be obtained[16]. If multiple particles are close in size, a longer SEC column or multiple cycles will be needed to purify the desired species[16]. SEC was used to isolate $Au_{30}(S\text{-}t\text{Bu})_{18}$ from the etched solution.

1.5: $Au_{30}(S\text{-}tBu)_{18}$ Crystal Structure

To understand the structure of $Au_{30}(S\text{-}t\text{Bu})_{18}$, single crystal X-ray diffraction studies (XRD) were explored. $Au_{30}(S\text{-}t\text{Bu})_{18}$ consists of a Au_{20} interpenetrating bicuboctahedral core that is capped by two Au atoms, forming the 22-atom core[1,3]. This 22-atom core is protected by six bridging units, two monomeric staples, and two trimeric staples[1,3]. A bridging unit is a thiolate ligand connected directly to the Au core. The two monomeric staples [RS-Au-SR], and two trimeric staples [RS-Au-SR-Au-SR-Au-SR] make up the additional eight gold atoms surrounding the Au_{22} core. In total, the twenty-two gold core atoms and the eight staple gold atoms make up the thirty gold atoms in $Au_{30}(S\text{-}t\text{Bu})_{18}$ structure. The thiolate ligand used in $Au_{30}(S\text{-}t\text{Bu})_{18}$ is *tert*-butylthiol[1,3]. S-*t*Bu is in the class of bulky ligands and consists of a thiol attached to a *tert*-butyl carbon group[7]. The

structural shape of S-*t*Bu will be further discussed in comparison to phenylethanethiol, PC2, in future chapters.

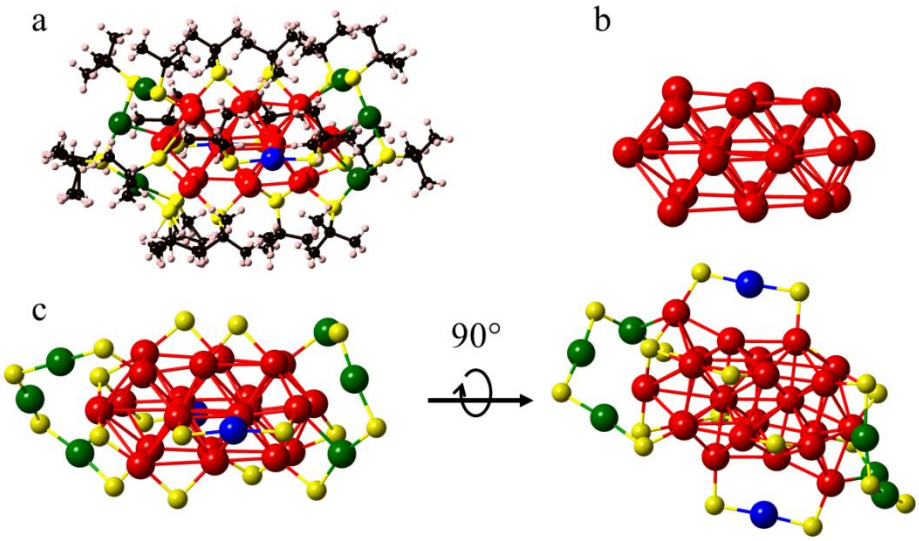

Figure 1.4: Crystal structure of Au_{30}(S-*t*Bu)$_{18}$ showing (a) the full $Au_{30}((CH_3)_3CS)_{18}$ structure, (b) the Au_{22} bicuboctahedral core, and a (c) 90-degree rotational view of $Au_{30}S_{18}$ staple motifs. The left side of (c) shows a view of the two trimeric staple motifs (green) and the right side of (c) shows a view of the two monomeric staple motifs (blue).

Chapter 2

Collision Induced Dissociation of $Au_{30}(S\text{-}tBu)_{18}$

2.1: Collision-Induced Dissociation (CID) Method

CID is a unique tool for determining the structural components of compounds through fragmentation[5]. Applying various Trap collision energies, molecules begin to break apart into smaller fragments of the parent ion upon collision with gas molecules in the Trap chamber. The order in which molecules, nanoclusters in this case, break apart provides insights into the structure and stability of the molecules. Using the MS/MS mode, particles of a specific mass are exclusively filtered and sent through the quadrupole of the ESI to detect their respective m/z. Unlike the MS mode that ionizes all molecules within a given m/z range, the MS/MS allows for the exclusive selection of one molecule size. Therefore, all CID peaks produced from the data collection can be confidently sourced back to the parent ion. In this study, CID data for $Au_{30}(S\text{-}t\text{Bu})_{18}$ was collected and compared to published CID data for $Au_{25}(SCH_2CH_2Ph)_{18}$. At this time, $Au_{25}(SCH_2CH_2Ph)_{18}$ is the only recorded AuNC to be studied in CID.

2.2: Experimental CID data for $Au_{30}(S\text{-}t\text{Bu})_{18}$

The collection of CID data for $Au_{30}(S\text{-}t\text{Bu})_{18}$ began with the mixing of the AuNC sample dissolved in toluene and diluted in HPLC grade THF. While the amount of HPLC-THF needed may vary, 50 µL of AuNC sample was generally mixed with 200 µL of HPLC-THF. If the AuNC solution is particularly concentrated, having a dark opaque color, more HPLC-THF will be needed. Once the mixed solution became a dark green, translucent color, the solution was extracted into a syringe and introduced to the ESI-MS via a capillary tube. To control the rate of sample injection into the machine, an AL-1000 syringe pump was used. The rate of the sample flow was maintained at a constant 0.3 µL/min.

To start data collection, the ESI-MS was run in the positive sensitive mode with a mass range window of 3000-8000 Da to identify the presence of the $Au_{30}(S\text{-}t\text{Bu})_{18}$ molecular mass peak. The MS-TOF mode was used for initial peak collection. The ESI device's Nanoflow+, TriWave, and Instrument setting values were periodically adjusted to maintain maximum ionization of the sample. In the Nanoflow+ module, the Capillary source value was set at 3.00 kV, Sample Cone at 120, and Source Offset at 15.0 during data collection. The temperature of the inner chamber was set to 110 degrees Celsius, and the Cone gas flow was set to 200 L/h. In the Triwave module, IMS Wave Velocity was set to 150 m/s and the Wave Height at 30.0 V. In the Instrument module, Trap gas was set at 6 mL/min. At this time, Trap and Transfer collision energies were turned off in the Instrument module.

After the presence of $Au_{30}(S\text{-}t\text{Bu})_{18}$ was seen in the mass spec data (m/z +1 at 7511.76 Da) and the degree of ionization became sufficient, CID collection was started. A high level of ionization, roughly <1.00E3, is important for high resolution CID data collection since the level of ionization is expected to decrease when the system is switched from the MS mode to the MS/MS mode. Therefore, a high starting ionization level is crucial. Once the proper setup is reached, the system is changed to the MS/MS mode and set to the mass of $Au_{30}(S\text{-}t\text{Bu})_{18}$ (7511.76 Da) seen previously in the MS mode. Setting the MS/MS mode to the exact mass of $Au_{30}(S\text{-}t\text{Bu})_{18}$ heavily narrows the mass filter and allows only $Au_{30}(S\text{-}t\text{Bu})_{18}$ to travel to the detector. The specificity of the MS/MS of $Au_{30}(S\text{-}t\text{Bu})_{18}$ in the data collection guarantees that all fragments seen during CID are due solely to the fragmentation of $Au_{30}(S\text{-}t\text{Bu})_{18}$. After the MS/MS mode is turned on and the mass value is set, the sample is ready to be run at varying Trap collision energies (CE). First, a base sample of the $Au_{30}(S\text{-}t\text{Bu})_{18}$ is run at 0V Trap CE to establish the parent ion peak. For CID collection, Transfer collision energy will remain off. In independent data collections, the $Au_{30}(S\text{-}t\text{Bu})_{18}$ is run

at 50V, 100V, 120V, 150V, and 200V Trap CE. Following collection, data for each Trap CE voltage increment was overlayed in ascending order to view the fragmentation of $Au_{30}(S\text{-}t\text{Bu})_{18}$.

2.3: Discussion of $Au_{30}(S\text{-}tBu)_{18}$ CID data

Following the outline of the $Au_{25}(SCH_2CH_2Ph)_{18}$ study, CID data for $Au_{30}(S\text{-}tBu)_{18}$ was collected. While increasing Trap collision energies in increments of 50V, 100V, 120V, 150V, and 200V, $Au_{30}(SR)_{18}$ fragments were collected and identified. Overlaying the CID data in increasing Trap CE order shows the fragmentation of $Au_{30}(SR)_{18}$ into two species regions. At 50V trap CE, the parent ion is not the dominating species. Instead, $Au_{30}(SR)_{17}S$, a loss of one *tert*-butyl group, becomes the dominating species. At 100V Trap CE, the $Au_{30}(SR)_{17}S$ species becomes diminished and two broad $Au_{26}(X)_{13}$ and $Au_{30}(X)_{16}$ groups become the dominate species. X refers to the total number of -S and -S-*t*Bu groups. At 120V Trap CE, species peaks in the $Au_{26}(X)_{13}$ and $Au_{30}(X)_{16}$ regions begin isolating into fewer species as the upper $Au_{30}(X)_{16}$ species become diminished. At 150V Trap CE, species peaks narrow even further into two main peaks of $Au_{26}S_{10}$ and $Au_{30}S_{12}$. At this point all traces of the parent ion and upper $Au_{30}(X)_{18}$ regions are gone. At 200V Trap CE, the maximum voltage available, species peaks remain dominate with $Au_{30}S_{12}$ and $Au_{26}S_{10}$ while a new region appears at $Au_{29}S_{11\text{-}13}$.

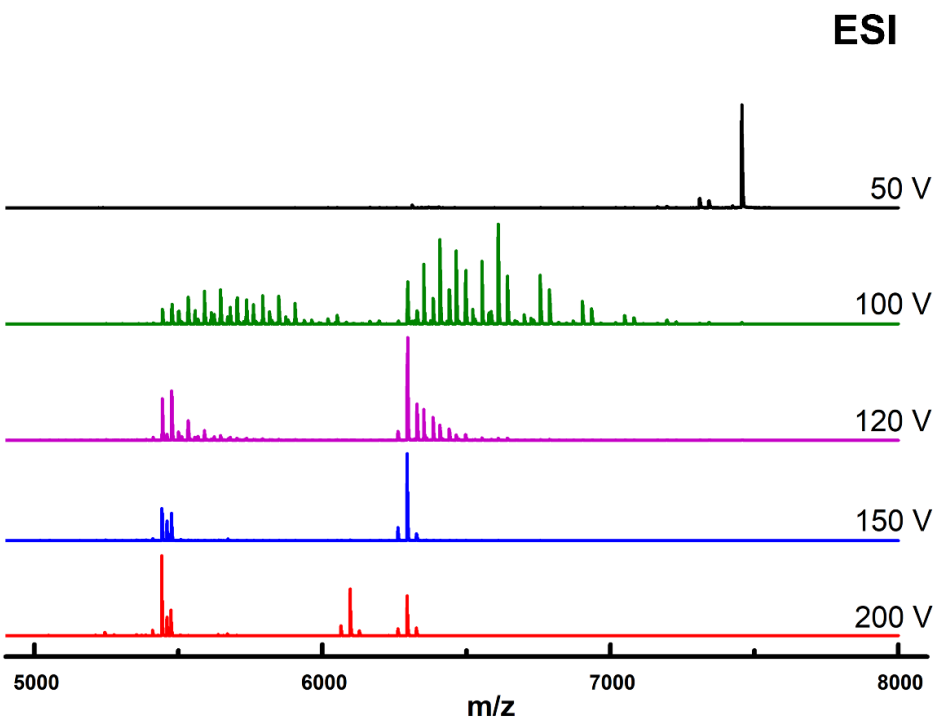

Figure 2.1: CID data of $Au_{30}(S\text{-}tBu)_{18}$ at 50V, 100V, 120V, 150V, and 200V Trap CE. At 50V Trap CE the largest peak shows $Au_{30}(S\text{-}tBu)_{17}S$. As Trap CE is increased to 100V, 120V, and 150V, two distinct fragment regions are formed: $Au_{26}(X)_{9\text{-}14}$ (left) and $Au_{30}(X)_{11\text{-}15}$ (right). Both fragment regions continue to narrow as Trap CE is increased until $Au_{26}S_9$ (left) and $Au_{30}S_{11}$ (right) are the major peaks present. At 200V Trap CE, a new fragment region appears for $Au_{29}S_{11\text{-}13}$.

2.4: Identifying peak fragments

After CID data was collected for $Au_{30}(S\text{-}tBu)_{18}$, each species peak was identified by chemical formula. In order to determine the identity of a peak fragment in ESI-MS/MS, two factors must be matched: formula mass and isotopic pattern. Formula mass is the matching of a compound's molecular mass to the m/z value of the peak. The m/z value, or mass-over-charge, represents the mass of the ionized particle divided by the charge of the particle[16]. For example, if a molecule

has a mass of 7000 Da and a charge of +1, the m/z value will be 7000. In contrast, if a molecule has a mass of 7000 Da and a charge of +2, the m/z value will be 3500. Therefore, once the charge state of the species is identified, the mass of the particle will be known. The charge state of a molecule can be determined by the m/z difference between isotope peaks. If the difference in m/z between isotope peaks is 1 Da, the species is identified as a +1. In comparison, if the difference in m/z between isotope peaks is 0.5 Da, the species is identified as +2. Charge states of +3, +4, +5, etc are also possible. However, for the current study, all peaks remained in the +1-charge state for $Au_{30}(S\text{-}t\text{Bu})_{18}$.

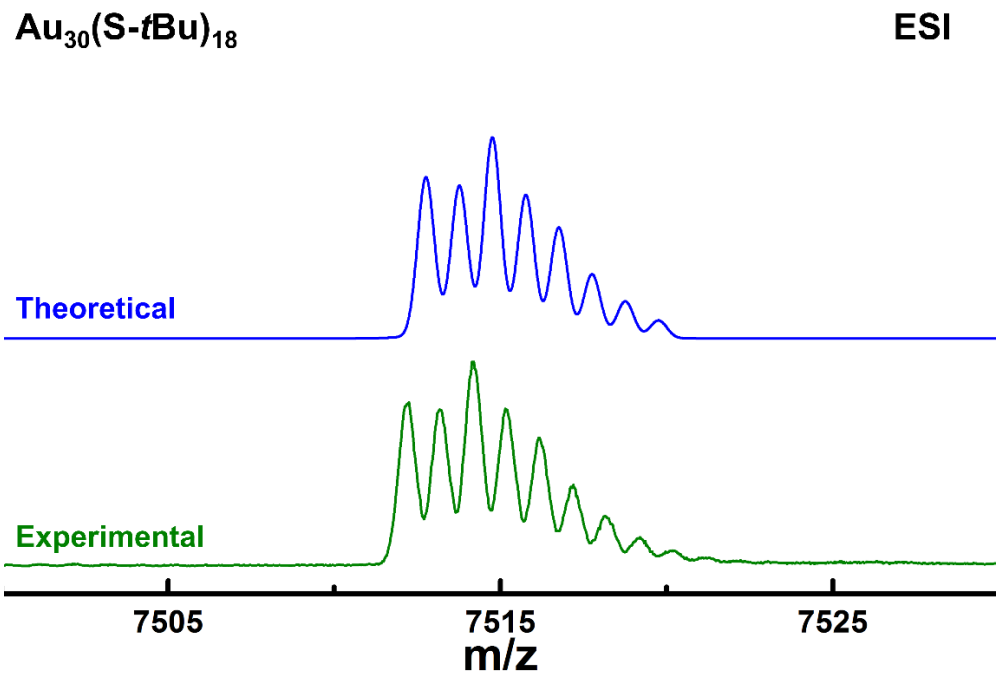

Figure 2.2: Isotope matching of $Au_{30}(S\text{-}t\text{Bu})_{18}$ peak in the experimental sample (green) with the software-generated theoretical peak (blue). Both the number and intensity of peaks match between experimental and theoretical, as well as the molecular mass of the nanocluster (+/- 1 Da). The matching of mass and isotope pattern confirms the identity of the ionized species.

The charge state of the ionized sample is vital to the collection of the mass spectroscopy data, especially during CID. For the time-of-flight data to be collected by the ESI-MS instrument, the molecule must be charged, and the sign of the charge being analyzed (+/-) must be preselected before data collection begins. Setting the ESI-MS to positive mode collects all positively charged ions while negative mode collects all negatively charged ions. Furthermore, if both positive and negative ions are in the sample, only one type of charge can be seen at a time. In the case of CID, the charge of species fragments is an important clue into missing pieces in the fragmentation puzzle. Since total charge remains constant for molecules during CID, different segments will retain different charges upon dissociation. In other words, if a species with a +1 charge were to be fragmented into two segments, one segment will retain a +1 charge and appear in the ESI-MS while the other will take on a neutral charge and not appear in mass spectrometry. Additionally, some fragments can even take on negative charges during dissociation. Therefore, accounting for neutral and oppositely charged species fragments is necessary during fragmentation analysis. In the study of $Au_{25}(SCH_2CH_2Ph)_{18}$ CID, the frequent dissociation of $Au_4(SR)_4$ from the parent ion was not observed directly in the positive or negative mode but seen in the missing mass of larger species, since $Au_4(SR)_4$ maintains a neutral charge.

In addition to matching the suspected formula mass to the peak m/z value, the isotopic pattern must also be matched. The isotopic distribution of a compound is the chemical fingerprint of mass spectrometry. While two chemical formulas can have the same molecular mass (matching with the same m/z value), the isotopic distribution will differ. Using a theoretical isotopic distribution calculator in the ESI software, any suspected formula for a peak identity can have an isotopic distribution generated and overlaid on top of the experimental peaks. If the isotopic

pattern and m/z pattern match, the identity of the experimental peak can be claimed with confidence.

2.4.1: MatLab Peak Probability Software

While the chemical formula of ESI-MS peaks can be manually calculated, MatLab programs provide a faster way to determine peak identities. When large AuNCs, such as $Au_{30}(S\text{-}t\text{Bu})_{18}$, are fragmentized in CID, resulting fragments can consist of any number of gold, thiol, and sulfur combinations. Instead of guessing the combination of the resulting fragment, each combination of the potential fragment can be analyzed given a specific mass range. For this study, we will look at the use of MatLab to identify $Au_{30}(S\text{-}t\text{Bu})_{18}$ fragments. To start the process, the number of variables and maximum number of variable quantities are input into the software. Since CID fragments must consist of some part of the original $Au_{30}(S\text{-}t\text{Bu})_{18}$ molecule, the variables will include Au, S-*t*Bu, and S. The difference between S-*t*Bu and S is for when the *tert*-butyl group of the tertiary butylthiol is lost but the S remains attached to Au. Using the starting formula of the parent molecule, the maximum number of Au, S-tBu, and S are 30, 18, and 18 respectively. Next, a given mass range of the unknown is input, usually +/- 10 Da from the unknown peak value. Finally, a list of potential formula combinations that fall into the mass range are displayed and can be checked using the isotopic generator in the ESI.

2.4.2: The Left Bump Problem

As the CID fragment peaks of $Au_{30}(S\text{-}t\text{Bu})_{18}$ were identified, a particular problem in matching isotopic patterns occurred. When viewing the isotopic distribution of the experimental CID, a small but noticeable left peak appeared on some of the fragment isotopes at 100 and 120V Trap CE. This left most peak, or left bump, created great difficulty when trying to match theoretical

formulas with experimental peaks. Since all fragments of $Au_{30}(S\text{-}tBu)_{18}$ are assumed to only contain Au, S-tBu, or S, the presence of a small left isotope peak was theoretically impossible, for none of the three components contain a small isotope pattern on the left side (low mass side). It was thought that some contamination was occurring in the machine, leading to the addition of Fe or Zn to the species fragments. The thought was that Fe or Zn, which contain a small left peak in their isotope distribution, may be attaching to the AuNC fragments and leading to the problem; however, the left bump also varied in peak height among different peaks and various Trap collision energies.

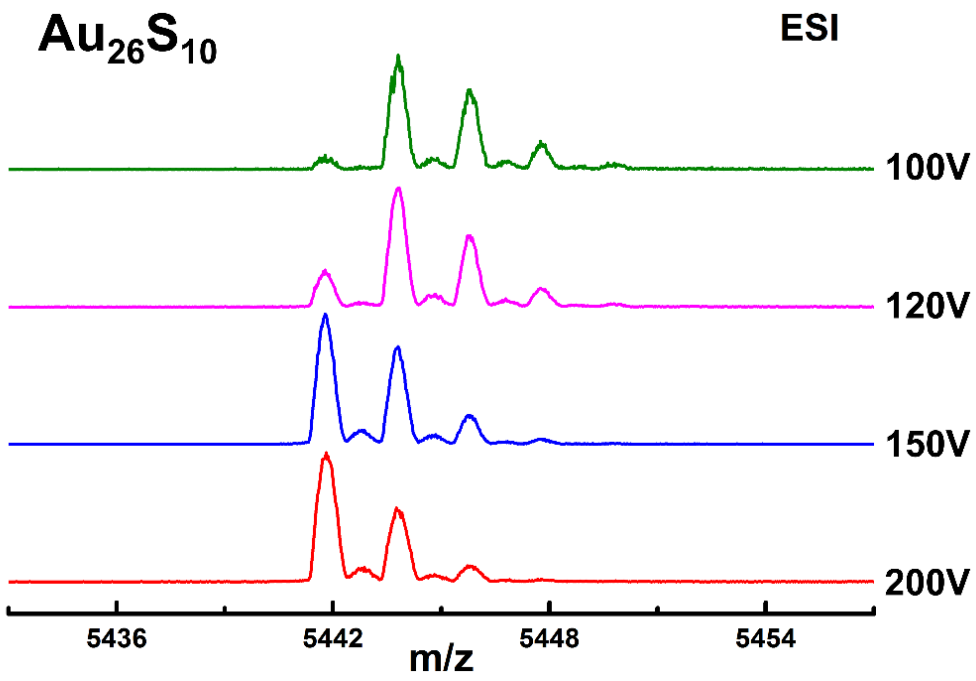

Figure 2.3: Isotopic distribution of a $Au_{26}S_{10}$ fragment at 100V, 120V, 150V, and 200V Trap CE to demonstrate the left bump. At 100V, the major three isotopic peaks of $Au_{26}S_{10}$ appear in descending order with a small isotope peak visible on the left side of the tallest peak. When Trap CE is increased, the left bump seen at 100V increases in intensity until becoming the major

isotope peak at 200V. At the same time, the right most peak of $Au_{26}S_{10}$ decreases in intensity as Trap voltage increases until no peak is visible at 200V.

Finally, a pattern was noticed among left bump peaks as Trap collision energy was increased. As seen in Figure 2.3, overlaying the same peak at multiple Trap collision energies (100V, 120V, 150V, and 200V), shows the left bump growing in height as Trap CE is increased. In fact, the left bump grows in height until the left peak becomes the main peak of isotope pattern. With this new revelation, it was determined that the left bump was in fact another species, varying by two hydrogens, overlayed on top of the main species. Depending on the voltage of the Trap, one of the two species predominated in composition and the other, smaller in intensity, hid behind the isotopic pattern and created only a small peak on the low mass side of the isotope. As Trap CE, was increased, the species containing two less hydrogens became more and more dominate until it showed as the main isotopic peak with a small right bump from the other species.

The conclusion of the left bump problem provided much needed clarity in the identification of $Au_{30}(S\text{-}t\text{Bu})_{18}$ fragment peaks as well providing insight into the fragmentation of the parent ion. Now that the addition of hydrogen atoms was known, new questions about the source of the hydrogens and the location in which they attach to the fragment species came about. It is thought that the hydrogen atoms may be bonding to the open sulfur atoms of the fragment species. As will be discussed in further detail later, the carbon group of the S-*t*Bu ligand in $Au_{30}(S\text{-}t\text{Bu})_{18}$ appear to cleave during fragmentation, resulting in a remaining S atom attached to the gold core. With the sulfur atom exposed, a hydrogen may bind to the sulfur and create a simple thiol. However, this solution does not explain why the two overlapping species always vary by 2 Da (2 hydrogens). Further discussion is needed on why two hydrogens must always attach instead of a single hydrogen.

2.5: Discussion of $Au_{30}(S\text{-}tBu)_{18}$ vs $Au_{25}(SCH_2CH_2Ph)_{18}$ CID

When comparing the CID data collected for $Au_{30}(S\text{-}t\text{Bu})_{18}$ to data published for $Au_{25}(SCH_2CH_2Ph)_{18}$, two distinctly different fragmentation patterns can be seen. Data collected on $Au_{25}(SCH_2CH_2Ph)_{18}$ CID fragmentation shows a linear progression of decreasing fragment size with increasing Trap CE[5]. In other words, the dominant species went from the parent ion $Au_{25}(SR)_{18}$ to $Au_{21}(X)_{14}$, to $Au_{17}(X)_{10}$, to Au_{13} as the Trap CE increased from 50V, to 100V, to 120V, to 150V respectively. In contrast, the stable species fragments of $Au_{30}(S\text{-}t\text{Bu})_{18}$ did not follow such a linear pattern with increasing Trap CE. Instead, $Au_{30}(S\text{-}t\text{Bu})_{18}$ fragments became isolated between two major peaks at $Au_{26}S_{10}$ and $Au_{30}S_{12}$. These two isolated peaks remained even when maximum Trap CE, 200V, was applied.

While the fragmentation patterns of $Au_{30}(S\text{-}t\text{Bu})_{18}$ and $Au_{25}(SCH_2CH_2Ph)_{18}$ appear to vary as Trap CE is increased, the two nanoclusters may share the same initial loss of $Au_4(SR)_4$ during initial collision. For $Au_{25}(SCH_2CH_2Ph)_{18}$, the parent ion first fragments by losing a $Au_4(SR)_4$ group which results in the fragment species $Au_{21}(X)_{14}$[5]. For $Au_{30}(S\text{-}t\text{Bu})_{18}$, the parent ion also shows a similar loss of $Au_4(SR)_4$ without any fragment species between 26 and 30 Au atoms. The lack of transition fragments between species of 26 and 30 Au atoms supports the theory that $Au_4(SR)_4$ is lost from the $Au_{30}(S\text{-}t\text{Bu})_{18}$ structure at some point in the fragmentation.

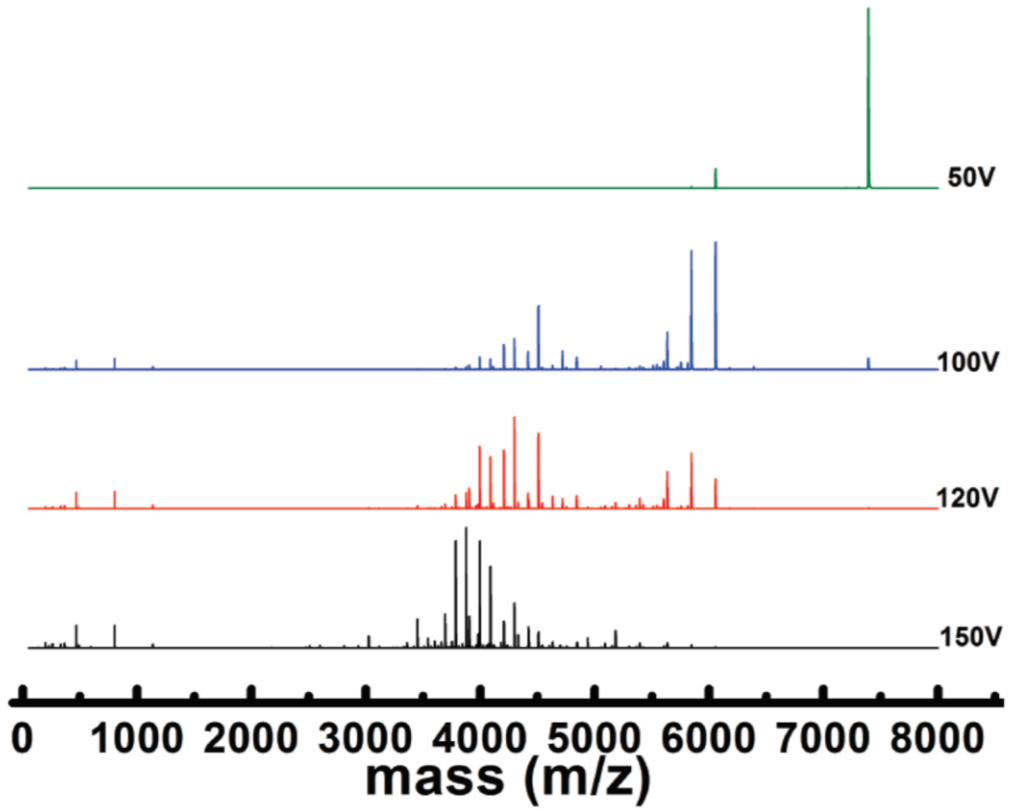

Figure 2.4: CID data of $Au_{25}(SCH_2CH_2Ph)_{18}$ at 50V, 100V, 120V, and 150V Trap CE collected by Dr. Angel and colleagues. At 50V, $Au_{25}(SCH_2CH_2Ph)_{18}$ is the largest peak present[5]. As Trap CE is increased to 100V, $Au_{21}(X)_{14}$ appears as the tallest peak with some $Au_{17}(X)_{10}$ present in the lower mass region[5]. At 120V, $Au_{17}(X)_{10}$ is the dominant species present[5]. Lastly, Au_{13} core fragments appear as the tallest peaks at 150V Trap CE[5]. Reprinted (adapted) with permission from Angel, L. A.; Majors, L. T.; Dharmaratne, A. C.; Dass, A. Ion Mobility Mass Spectrometry of $Au_{25}(SCH_2CH_2Ph)_{18}$ Nanoclusters. ACS Nano 2010, 4 (8), 4691–4700. Copyright 2022 American Chemical Society.

Chapter 3

Ion Mobility Mass Spectrometry (IM-MS) of $Au_{30}(S\text{-}tBu)_{18}$

3.1: IM-MS/MS

IM-MS/MS provides drift time data that can be useful for determining the shapes and structures of unknown particles[5]. While mass spectrometry is useful for finding the compositional identity and intensity of ionized particles, IM-MS/MS can give insights into the 3D-dimensional structure and distribution of atoms[5]. By analyzing the drift time of particles in relation to their m/z value, molecules or isomers of the same mass can be distinguished by varying drift time[5]. Drift time is the time it takes the ionized molecule to pass through the ion-mobility separation section of the Triwave. See Figure 3.1 for the location of the Triwave. The time it takes the ionized molecules to travel through the gas filled chamber and reach the detector, or drift time, is directly dependent on the cross-sectional area of the molecule. As molecules increase in cross-sectional area, they become more hindered when traveling through the buffer gas[5]. Larger molecules collide much more readily with gas molecules in the separation chamber than smaller molecules, causing them to slow down with each collision. The more hindered the molecule becomes, the greater the drift time. Consequently, a molecule with fewer atoms and a large cross-sectional area can have the same drift time as a molecule with more atoms but a smaller cross-sectional area.

The use of IM-MS/MS methods in identifying structural components of gold nanoclusters is a new and promising field[5]. By collecting the IMS data from the CID of AuNCs, the drift times of resulting fragments can help determine the order of dissociation. As the thiolate ligand monolayer of AuNCs is fragmentized, the AuNC becomes increasingly less bulky and therefore has a smaller cross-sectional area. As the cross-sectional area decreases, the drift time of the AuNC fragment also decreases. The use of IM-MS/MS to determine the structural composition of AuNCs is particularly important for molecules that are unable or yet to be crystallized. The current method of sc-XRD requires the crystallization of AuNCs to determine the exact arrangement of the core

and thiolate monolayer; however, crystallization has proven difficult for many nanocluster species, making the crystal structure inaccessible for XRD. By determining drift time patterns in the dissociation of AuNCs, IMS could one day be used as a tool to determine the structure of particles that do not crystallize well.

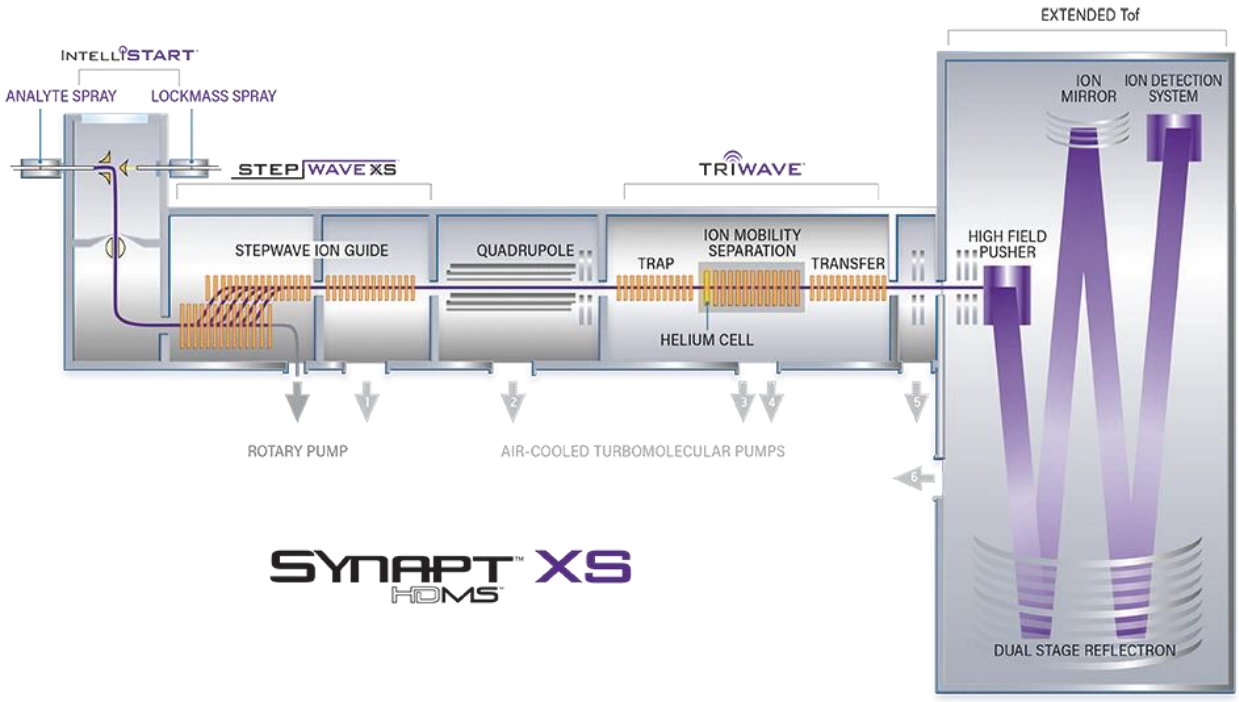

Figure 3.1: Overview of the Synapt XS device used for ESI-MS, CID, and IM-MS/MS data collection. CID of AuNCs occurs in the Trap portion of the TriWave chamber. After exiting the Trap tube, AuNCs enter the Ion Mobility Separation tube and drift time data is collected. The Extended TOF portion of the Synapt XS applies kinetic energy to the AuNC sample and records time-of-flight data for m/z calculation. https://www.waters.com/waters/en_US/SYNAPT-XS-High-Resolution-Mass-Spectrometer/nav.htm?cid=135020928&locale=en_US

3.2: Experimental IM-MS/MS data for $Au_{30}(S\text{-}tBu)_{18}$

The collection of IM-MS/MS data follows the same beginning steps as the CID data collection process. Following the identification of the $Au_{30}(S\text{-}t\text{Bu})_{18}$ parent ion in the MS mode, the system is then switched to the MS/MS mode and data is collected at varying Trap CEs; however, unlike the CID method, an additional step of ion mobility separation is added to find the drift time values of the AuNC fragments. In the Acquisition Mode module, TOF is switched to Mobility TOF to begin the drift time collection. The TOF viewing window should show a peak of the distribution of drift times in the sample. To collect clear drift time data of the sample, the distribution peak must be narrow and not flare at the bottom of the peak. If flaring occurs, a broad drift-time line will appear in the IM-MS data and the exact drift time of the AuNC fragment will be uncertain. To address this problem, Transfer CE can be turned on and increased until the TOF distribution peak narrows. It is important to note that increasing the Transfer CE too much may skew the distribution of the species seen in the mass spectrum.

Once the TOF distribution is set, IMS collection of $Au_{30}(S\text{-}t\text{Bu})_{18}$ is ready. Similar to the CID method, the sample was run at increasing Trap CE values of 0V, 50V, 100V, 120V, 150V, and 200V; however, all Trap CE changes were done in the same data collection trial. To divide the collection of varying Trap CE fragments equally, each mentioned Trap CE was run for 3 minutes, changing the voltage after the allotted time while continuing the data collection. If ionization levels are low or higher data resolution is desired, the time of each voltage interval can be increased. The amount of time in each interval will have no effect on the number of ionized peaks seen, but it will effect the resolution of the mass peaks. Following collection, IMS data can be viewed by uploading the data file into DriftScope software.

3.3: Discussion of $Au_{30}(S\text{-}tBu)_{18}$ IM-MS data

IMS data was collected for $Au_{30}(S\text{-}tBu)_{18}$ to show the relationship between drift time and mass-per-charge of resulting CID fragments. The Driftscope plot of $Au_{30}(S\text{-}tBu)_{18}$, Figure 3.2, shows two distinct bands that decrease in drift time with decreasing mass. The topmost band of $Au_{30}(S\text{-}tBu)_{18}$ embodies fragments of $Au_{30}(X)_{11\text{-}18}$. In this band, the highest fragment begins with all initial thiolate ligands and systematically loses -*t*Bu and -S groups until reaching eleven ligands and all initial Au atoms. The bottommost band of $Au_{30}(S\text{-}tBu)_{18}$ fragments embodies $Au_{26}(X)_{9\text{-}14}$. In this band, the highest fragment begins with a loss of $Au_4(SR)_4$. Similar to band 1, band 2 systematically loses -R and -S groups until reaching nine ligands and twenty-six Au atoms.

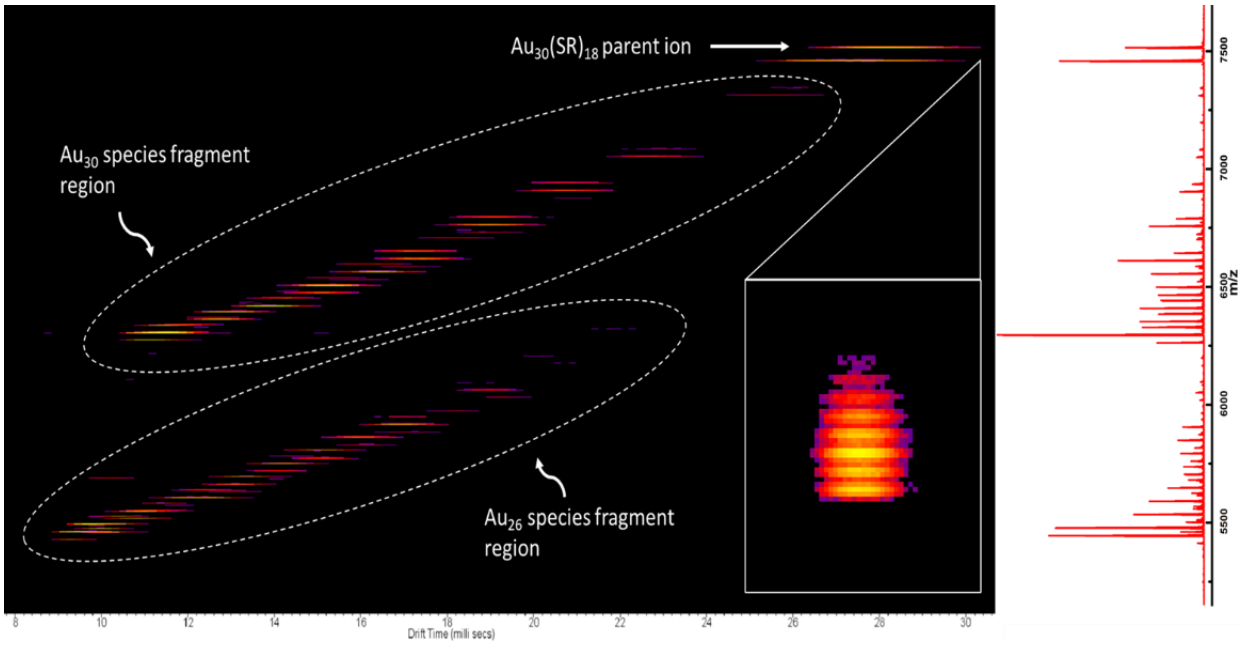

Figure 3.2: IM-MS/MS drift time data for $Au_{30}(S\text{-}tBu)_{18}$ showing (a) the $Au_{30}(SR)_{18}$ parent ion as well as two distinct fragment regions: (b) Au_{30} region and (c) Au_{26} region. The two positively sloped bands represent the incremental decrease in drift time as -*t*Bu and -S groups detach from the thiolate protecting monolayer of the AuNCs.

Ionization of the Au_{20} core or subsequent fragments after $Au_{26}(X)_9$ were unable to be achieved in IMS positive mode. One reason for the lack of small ionization could be due to an inherent neutral or negative charge of the fragments. $Au_{30}(S\text{-}t\text{Bu})_{18}$ does not readily ionize in the negative mode, making it difficult to collect data from both +/- viewpoints.

3.3.1: Discussion of $Au_{30}(S\text{-}tBu)_{18}$ vs $Au_{25}(SCH_2CH_2Ph)_{18}$

When comparing IM-MS/MS data of $Au_{30}(S\text{-}t\text{Bu})_{18}$ to published data on $Au_{25}(SCH_2CH_2Ph)_{18}$, two differing patterns occur. Continuing the discussion seen in the CID data section, $Au_{30}(S\text{-}t\text{Bu})_{18}$ isolates into two species regions, while $Au_{25}(SCH_2CH_2Ph)_{18}$ systematically dissociates from the parent ion to the Au_{13} core[5]. The IMS drift time data also supports these differences by showing two distinct fragment bands in $Au_{30}(S\text{-}t\text{Bu})_{18}$, while only showing one descending band in $Au_{25}(SCH_2CH_2Ph)_{18}$. The differences in drift time patterns between $Au_{30}(S\text{-}t\text{Bu})_{18}$ and $Au_{25}(SCH_2CH_2Ph)_{18}$ mimic the observations seen in CID while also giving insight into how the structure of the AuNCs is changing as dissociation occurs.

One of the major differences in drift time patterns seen between the two AuNCs is the lack of small fragment bands inside the large bands of $Au_{30}(S\text{-}t\text{Bu})_{18}$. In the IMS drift time data of $Au_{25}(SR)_{18}$, eight distinct bands run perpendicular to the trendline of the large main band[5]. Each of the small eight bands contains fragments of $Au_{25}(SR)_{18}$ that vary in Au, SR, and S. The main reason for the lack of bands in $Au_{30}(S\text{-}t\text{Bu})_{18}$ is due to the consistency of Au atoms across all fragments in the band. When sulfur and thiol groups are systematically lost from the parent ion, the drift time of the molecules does not change drastically, rather in small steps. The loss of a -*t*Bu groups create a moderate decrease in drift time, due to the decrease in cross-sectional area when the carbon group of the thiol detaches. The loss of a -S group creates a smaller decrease in drift time, due to the small contribution that the S atom has on the cross-sectional area. Au

atoms, however, are large and significantly affect the cross-sectional area when lost, making the drift time decrease the most. Therefore, since $Au_{30}(S\text{-}t\text{Bu})_{18}$ fragments only lose -*t*Bu, -S-*t*Bu, and -S groups in each major band, there will only be one band fragment, instead of multiple perpendicular bands like in $Au_{25}(SCH_2CH_2Ph)_{18}$.

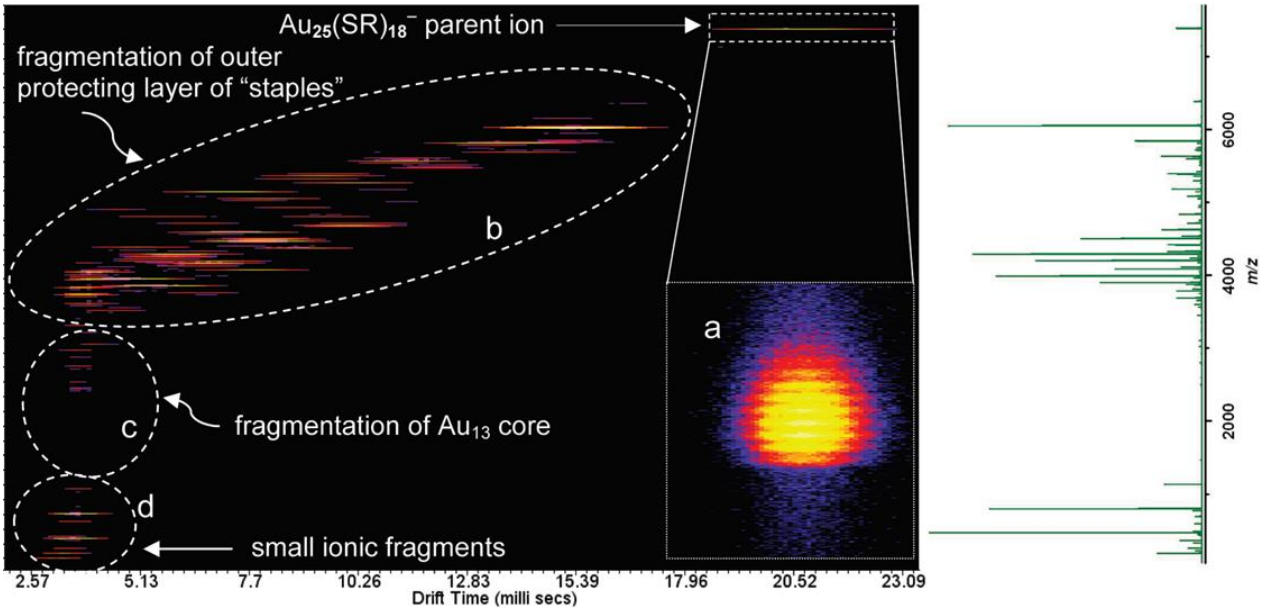

Figure 3.3: IM-MS/MS drift time data for $Au_{25}(SCH_2CH_2Ph)_{18}$ collected by Dr. Angel and colleagues showing (a) the $Au_{25}(SR)_{18}$ parent ion, (b) fragmentation region consisting of Au_{21} and Au_{17} species, (c) fragmentation of Au_{13} core, and (d) smaller ionized fragments. The single, positively sloped (b) fragment region represents the incremental loss of both Au_4SR_4 staples and the thiolate protecting monolayer. Reprinted (adapted) with permission from Angel, L. A.; Majors, L. T.; Dharmaratne, A. C.; Dass, A. Ion Mobility Mass Spectrometry of $Au_{25}(SCH_2CH_2Ph)_{18}$ Nanoclusters. ACS Nano 2010, 4 (8), 4691–4700. Copyright 2022 American Chemical Society.

Fragmentation of the Au_{20} core during $Au_{30}(S\text{-}t\text{Bu})_{18}$ dissociation was not seen in IM-MS drift time data. The lack of core fragments in the IMS drift time can be due to two reasons: either the

fragments were there but negatively or neutrally charged, or no fragments dissociated the core further than seen. In the first option, fragmentation of the core could create fragments containing charges that are not picked up in the positive mode, such as negatively charged or neutrally charged molecules. After drift time data was collected for $Au_{25}(SCH_2CH_2Ph)_{18}$, IM-MS and CID experiments were run in both positive and negative mode to see all the fragments available; however, since $Au_{30}(S\text{-}t\text{Bu})_{18}$ does not readily ionize in the negative mode, collection of negatively charged fragments was not available[5]. In the second option, the stability of the $Au_{30}(S\text{-}t\text{Bu})_{18}$ core may allow the AuNC to remain intact even in the presence high collision energy. It is already seen that the Au_{20} core of $Au_{30}(S\text{-}t\text{Bu})_{18}$ is stable enough to lose most of the supporting thiolate ligand monolayer before losing any Au atoms, so the possibility of the $Au_{30}(S\text{-}t\text{Bu})_{18}$ fragments remaining mostly together cannot be dismissed. More experiments will need to be run to look for further $Au_{30}(S\text{-}t\text{Bu})_{18}$ dissociation.

Chapter 4

Fragmentation series of $Au_{30}(S\text{-}tBu)_{18}$

4.1: Fragmentation series method

Though mass spec helps to reveal the identities of fragment species and IM-MS/MS helps to show the bulkiness of each fragment, the order in which the fragments dissociate from the parent ion still remains a mystery. To further explain, the mass spectrometry of CID fragments orders each fragment by m/z value, not by order in which that fragment dissociated. Therefore, adjacent peaks that differ only by one S atom do not necessarily mean that one species lost a single S atom and became species 2. To determine the actual order, or theoretically assumed order, the identity of all CID peaks must be collected and evaluated for patterns.

Patterns of identified peaks can be seen in a variety of ways. One particular method is looking at the major species fragment regions at varying Trap CEs. It is seen that as Trap CE increases, more and more smaller species fragments appear in ionization. In this logic, as the energy applied to the parent ion is increased, more and more layers of the outer thiolate monolayer and staple groups are removed from the AuNC. Therefore, looking at the identities of species at differing Trap voltages can clue into the order of dissociation.

a)

$$[Au_{25}SR_{18}] \longrightarrow [Au_{21}X_{14}] + [Au_4SR_4] \longrightarrow [Au_{17}X_{10}] + [Au_4SR_4] \longrightarrow [Au_{13}\ \text{core}]$$

b)

$$[Au_{25}SR_{18}] \longrightarrow [Au_{25-x}X_{18-(x+1)}] + [Au_x(SR)_{x+1}]$$

Figure 4.1: The proposed fragmentation series of $Au_{25}(SCH_2CH_2Ph)_{18}$ as described by Dr. Angel and colleagues. The extended formula (a) shows the three consecutive losses of $Au_4(SR)_4$ from $Au_{25}(SCH_2CH_2Ph)_{18}$ until only the Au_{13} core remains. A condensed formula (b) is also included for simplification.

To explain this method, the fragmentation of $Au_{25}(SCH_2CH_2Ph)_{18}$ will be described. After applying increasing levels of Trap CE to $Au_{25}(SCH_2CH_2Ph)_{18}$, it was seen that new species regions appeared with each increasing increment of collision energy[5]. In fact, each new species region was seen to be a smaller fragment than the previous collision energy fragment region, implying a sequential fragmentation series. At 50V Trap CE, the parent ion remained as the main species peak, but a small peak identified as $Au_{21}(X)_{14}$ was seen lower in the mass spectrum[5]. The presence of $Au_{21}(X)_{14}$ shows that at 50V Trap CE, the parent ion is largely stable but begins dissociation by releasing a $Au_4(SR)_4$ piece from the main structure[5]. As Trap CE is increased to 100V, the $Au_{21}(X)_{14}$ species becomes the dominating species and a new species region identified as $Au_{17}(X)_{10}$ appears[5]. The formation of $Au_{17}(X)_{10}$ represents another loss of $Au_4(SR)_4$ from the parent ion following the creation of $Au_{21}(X)_{14}$[5]. Continuing the pattern, as Trap CE was increased to 120V, $Au_{17}(X)_{10}$ became the dominate species and the formation of Au_{13} fragments appeared[5]. Au_{13} fragments were seen to come from another loss of $Au_4(SR)_4$ from the parent ion[5].

Using the identified species regions of $Au_{25}(SCH_2CH_2Ph)_{18}$ at increasing collision energies, a final fragmentation series was made. The series follows as $Au_{25}(SR)_{18}$, to $Au_{21}(X)_{14}$, to $Au_{17}(X)_{10}$, to Au_{13} core, as seen in Figure 4.1[5]. The fragmentation series of $Au_{25}(SR)_{18}$ showed three consecutive losses of $Au_4(SR)_4$ until only the Au_{13} core remained[5]. Using the crystal structure of $Au_{25}(SCH_2CH_2Ph)_{18}$ to explain the source of the fragments, it was theorized that the $Au_4(SR)_4$ fragments came from the joining of two dimeric staples of the parent ion that formed a cyclic ring and broke off from the main structure[5]. In each $Au_{25}(SCH_2CH_2Ph)_{18}$ molecule, there are six dimeric staple motifs surrounding the Au_{13} core. The fusion of two of the dimeric staples creates the $Au_4(SR)_4$ ring that is seen to fragment in the series. With six dimeric staples and two staples

per ring $Au_4(SR)_4$ ring, the three losses of $Au_4(SR)_4$ seen in the fragmentation series are strongly supported by the $Au_{25}(SCH_2CH_2Ph)_{18}$ crystal structure.

4.2: Fragmentation series of $Au_{30}(S\text{-}tBu)_{18}$

When evaluating the fragmentation series of $Au_{30}(S\text{-}t\text{Bu})_{18}$, patterns similar to that of $Au_{25}(SCH_2CH_2Ph)_{18}$ did not appear. As discussed in the CID and IMS sections, $Au_{30}(S\text{-}t\text{Bu})_{18}$ does not appear to follow a linear fragmentation series. Instead, the AuNC shows a branched series of Au_{30} and Au_{26} fragment regions that progressively lose protecting ligands while maintaining the gold core stability. The method used to determine the fragmentation series of $Au_{25}(SCH_2CH_2Ph)_{18}$ has not shown to be effective in understanding $Au_{30}(S\text{-}t\text{Bu})_{18}$ fragmentation. Unlike the sequential fragmentation seen with $Au_{25}(SCH_2CH_2Ph)_{18}$, $Au_{30}(S\text{-}t\text{Bu})_{18}$ does not gain new species regions with each increasing increment of Trap CE following the initial creation of the Au_{30} and Au_{26} regions. The species regions of $Au_{30}(S\text{-}t\text{Bu})_{18}$ instead become more narrowed with each increase in Trap CE. Therefore, a new approach to understanding the fragmentation of $Au_{30}(S\text{-}t\text{Bu})_{18}$ must be used.

To further understand the order of $Au_{30}(S\text{-}t\text{Bu})_{18}$ fragmentation, a graph of ligand number vs. thiol number was made to chart every identified fragment peak from the CID data. As seen in Table 4.1, Total ligand number represents the combined number of thiol groups (S-*t*Bu) and sulfur groups that have lost their *tert*-butyl carbons (S). The thiol number represents only the number of thiols (S-*t*Bu) on the species fragment. By combining all the identified peaks into one graph, a full picture of $Au_{30}(S\text{-}t\text{Bu})_{18}$ can be seen.

Table 4.1: The breakdown series is a collection of all identified species fragments from the CID of $Au_{30}(S\text{-}tBu)_{18}$. The y-axis shows the total ligand number (-S and -SR groups) and the x-axis shows the total thiol number (-SR). Au_{30} (blue) and Au_{26} (orange) species regions show no overlap in the same total ligand and thiol number among fragments. The most fragmented Au_{30} species identified was $Au_{30}S_{11}$ and the most fragmented Au_{26} species was $Au_{26}S_9$.

$Au_{30}(S\text{-}tBu)_{18}$ Breakdown Series										
Thiol #										
18	30,18,0									
17	30,17,1	30,17,0								
16										
15	30,15,3	30,15,2								
14										
13	30,13,5	30,13,4	30,13,3		26,13,1					
12					26,12,2					
11		30,11,6	30,11,5	30,11,4	26,11,3	26,11,2				
10					26,10,4	26,10,3				
9		30,9,8	30,9,7	30,9,6	26,9,5	26,9,4				
8			30,8,8	30,8,7	30,8,6	26,8,5	26,8,4			
7				30,7,8	30,7,7	26,7,6	26,7,5			
6					30,6,8	26,6,7	26,6,6	26,6,5		
5					30,5,9	30,5,8	26,5,7	26,5,6		
4						30,4,9	26,4,8	26,4,7		
3						30,3,10	26,3,9	26,3,8		
2						30,2,11	30,2,10	26,2,9		
1						30,1,12	30,1,11	26,1,10	26,1,9	
0						30,0,13	30,0,12	30,0,11	26,0,10	26,0,9
Total Ligand #	18	17	16	15	14	13	12	11	10	9

$Au_x(S\text{-}tBu)_yS_z = x,y,z$

The most prominent pattern seen in the breakdown series chart is the lack of species overlap between Au_{26} and Au_{30} species in the chart. While Au_{26} and Au_{30} species vary in thiol and sulfur count, no two species have been found to have the same number of thiol ligands and sulfurs attached. This lack of peak overlap is likely an indicator of the order in which $Au_{30}(S\text{-}t\text{Bu})_{18}$ fragments into Au_{30} and Au_{26} species regions. If the order of fragmentation was random, it is highly unlikely that none of the 31 identified Au_{30} fragments and 29 Au_{26} fragments would overlap in sulfur and thiol count.

4.2.1: $Au_{30}(S\text{-}tBu)_{18}$ fragmentation hypothesis 1

The first potential fragmentation series of $Au_{30}(S\text{-}t\text{Bu})_{18}$ is a single branched path. This "common ancestor" approach assumes that at one point in the fragmentation process, at around $Au_{30}(X)_{18}$, the AuNC can either continue losing sulfur and thiol groups or lose a $Au_4(SR)_4$ group and then continue losing sulfur and thiol groups. In this option, all Au_{26} fragment species come from the further dissociation of $Au_{26}(X)_{14}$. The benefit of this method is that it shows a clear point in the fragmentation in which $Au_{30}(X)_{18}$ becomes $Au_{26}(X)_{14}$, similar to the loss of $Au_4(SR)_4$ in the fragmentation of $Au_{25}(X)_{18}$ to $Au_{21}(X)_{14}$.

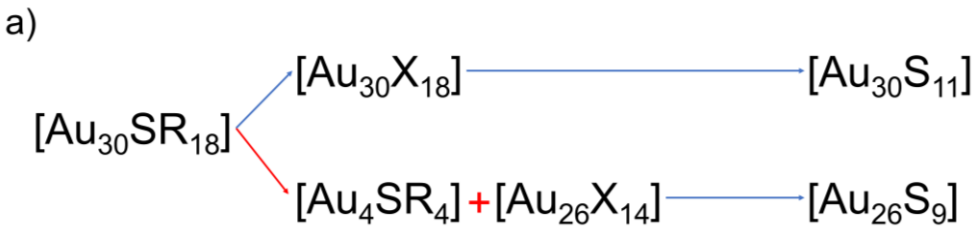

Figure 4.2: Fragmentation hypothesis 1 shows a common ancestor approach to $Au_{30}(S\text{-}t\text{Bu})_{18}$ dissociation. In this method, $Au_{30}(S\text{-}t\text{Bu})_{18}$ can either continually lose protecting thiolate ligands

until reaching $Au_{30}S_{11}$, or $Au_{30}(S\text{-}t\text{Bu})_{18}$ can lose an Au_4SR_4 group and then further dissociate the protecting monolayer until reaching $Au_{26}S_9$.

While this option is helpful in explaining the origin of the Au_{26} species region, it does not explain the non-overlap pattern seen in the series breakdown chart of $Au_{30}(S\text{-}t\text{Bu})_{18}$. If all Au_{26} fragments were to come from the further dissociation of $Au_{26}(X)_{14}$, it would be assumed that some of the lower mass species would share the same thiol and sulfur count of the Au_{30} species region fragments. For example, if $Au_{26}(SR)_{14}$ were to continuously lose SR, R, and S groups, it would be likely that eventually there would be a species of $Au_{26}(SR)_4S_9$, but only $Au_{30}(SR)_4S_9$ is seen. Therefore, more might be going on than a single branch.

4.2.2: $Au_{30}(S\text{-}tBu)_{18}$ fragmentation hypothesis 2

The second potential fragmentation series of $Au_{30}(S\text{-}t\text{Bu})_{18}$ is a multi-branched path. In this option, the $Au_{30}(S\text{-}t\text{Bu})_{18}$ parent ion loses a $Au_4(SR)_4$ group at varying points as it continuously loses the thiol and sulfur protecting groups. Once the $Au_4(SR)_4$ group has been lost, there is limited further fragmentation. The benefit of this is method is that it explains why there is no overlap in Au_{30} and Au_{26} species. Since all Au_{26} species come after the dissociation of Au_{30} thiol ligands, the Au_{26} species is not likely to have the same thiol and sulfur count.

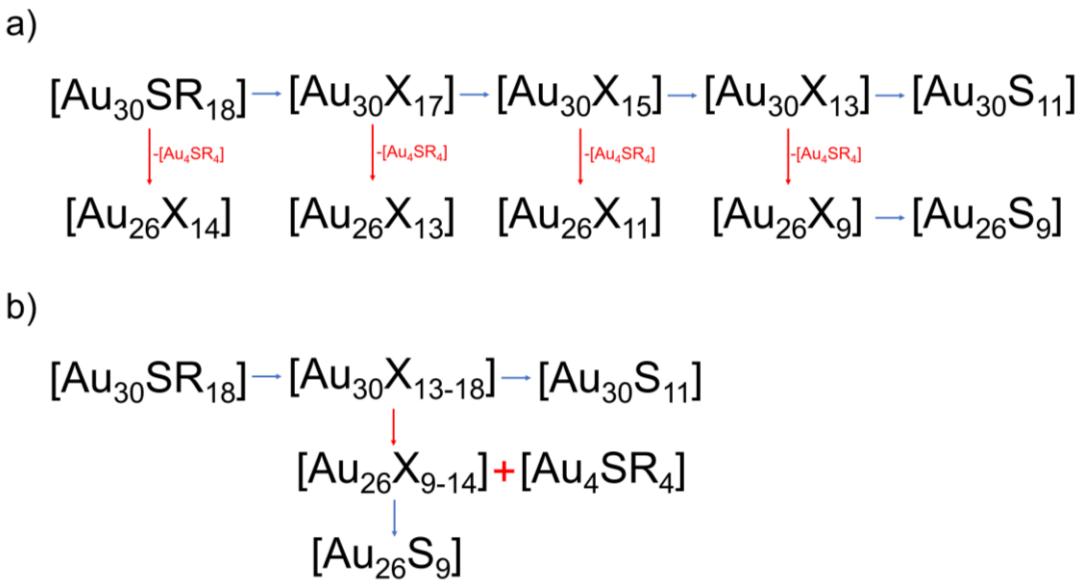

Figure 4.3: Fragmentation hypothesis 2 shows a multi-branched approach to $Au_{30}(S\text{-}tBu)_{18}$ dissociation. In this method, $Au_4(SR)_4$ can dissociate from the main $Au_{30}(S\text{-}tBu)_{18}$ structure at multiple points in the fragmentation process before further dissociating the protecting thiolate monolayer.

The main constraint of this option is the inability to explain when and how $Au_{30}(S\text{-}tBu)_{18}$ loses the 4 Au atoms. If the Au atoms can leave at multiple times in the fragmentation process, it becomes difficult to explain where the Au atoms are breaking off in the structure. Also, it does not explain why Au_{26} species could not further dissociate -SR and -S groups following initial collision.

4.3: Stability of thiol ligands in the fragmentation of $Au_{30}(S\text{-}tBu)_{18}$

Though the order of $Au_{30}(S\text{-}tBu)_{18}$ fragmentation is still unknown, the influence of the *tert*-butyl thiol ligand on the fragmentation process can still be seen. $Au_{30}(S\text{-}tBu)_{18}$ uses *tert*-butyl thiol, a bulky class ligand, as the protecting thiol monolayer. In comparison to the PC2, an aromatic class ligand used in $Au_{25}(SCH_2CH_2Ph)_{18}$, the *tert*-butyl of *tert*-butyl thiol forms a much more stable carbocation when cleaved from the sulfur atom. When the *tert*-butyl thiol becomes cleaved at the

sulfur atom, a tertiary carbocation is formed. In contrast, when PC2 becomes cleaved at the sulfur atom, a primary carbocation is formed. Due to the increased electron density on the tertiary carbocation, the *tert*-butyl carbocation is expected to be much more stable than the primary carbocation of the phenylethane carbocation. The degree of stability in ligand carbocations may explain the difference in fragmentation patterns between $Au_{30}(S\text{-}tBu)_{18}$ and $Au_{25}(SCH_2CH_2Ph)_{18}$.

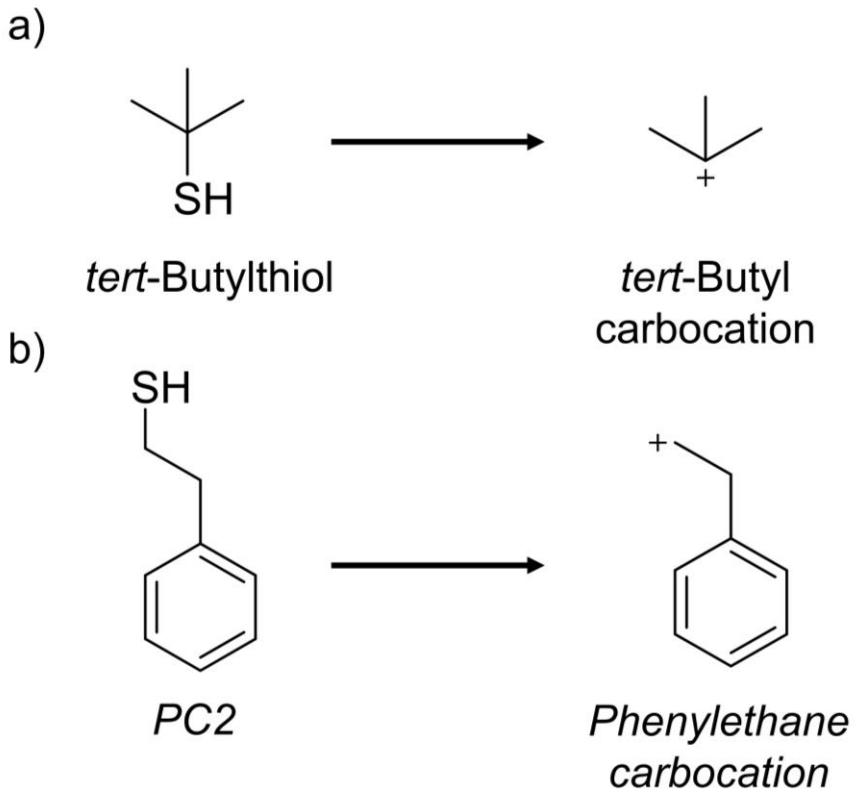

Figure 4.4: Formation of carbocations following S cleavage of (a) *tert*-Butylthiol and (b) PC2 thiol. The thiolate cleavage of (a) *tert*-Butylthiol forms a tertiary carbocation while (b) PC2 forms a primary carbocation. Tertiary carbocations display a greater stability than primary carbocations and may influence the higher loss of ligands in $Au_{30}(S\text{-}tBu)_{18}$ compared to that of $Au_{25}(SCH_2CH_2Ph)_{18}$.

As discussed in the CID and IM-MS/MS sections, $Au_{30}(S\text{-}tBu)_{18}$ loses all the R groups of the thiol protecting ligands in the Au_{30} region before any Au atoms are lost from the core or staples. The large loss of thiol carbon groups is not seen in the fragmentation of $Au_{25}(SCH_2CH_2Ph)_{18}$ and may be due to stability of the cleaved tertiary carbocation. Since the resulting fragment is stable, the AuNC can loss all *tert*-butyl groups before any further fragmentation occurs.

4.4: Conclusion

The CID and IM-MS/MS data of $Au_{30}(S\text{-}tBu)_{18}$ show unique dissociation patterns when compared to the only other studied nanocluster $Au_{25}(SCH_2CH_2Ph)_{18}$. Unlike the sequential and ordered breakdown of $Au_{25}(SCH_2CH_2Ph)_{18}$ from parent ion to gold core, $Au_{30}(S\text{-}tBu)_{18}$ demonstrates significant stability under high collision energy and maintains most of the starting Au atoms. CID of $Au_{30}(S\text{-}tBu)_{18}$ at 50V, 100V, 120V, 150V, and 200V Trap CE revealed the formation of two distinct fragment bands with no further fragmentation past $Au_{26}S_9$. Additionally, it was found that increasing Trap CE removed most of the *tert*-butyl groups from the parent ion with either no loss of Au or a single loss of $Au_4(SR)_4$. The large loss of -R groups with no loss in Au may be due to the weakness of the C-S bond in *tert*-butylthiol and the stability of the *tert*-butyl carbocation. IM-MS/MS drift time data of $Au_{30}(S\text{-}tBu)_{18}$ supported the hypothesis of a gradual loss in -R groups without any loss in gold by showing a linear slope of decreasing drift time with decreasing species mass. The drift time plot also provided clear evidence of the two species regions formed during $Au_{30}(S\text{-}tBu)_{18}$ fragmentation. Using a breakdown series plot of all identified $Au_{30}(S\text{-}tBu)_{18}$ CID fragments, two potential fragmentation series of $Au_{30}(S\text{-}tBu)_{18}$ were made. Though the two fragmentation hypothesizes vary in the order in which $Au_4(SR)_4$ is lost, both describe the loss of a an $Au_4(SR)_4$ group from the parent ion followed by the gradual loss of -S and -R groups from the protecting monolayer and Au/thiolate staples.

LIST OF REFERENCES

(1) Dass, A.; Jones, T.; Rambukwella, M.; Crasto, D.; Gagnon, K. J.; Sementa, L.; De Vetta, M.; Baseggio, O.; Aprà, E.; Stener, M.; Fortunelli, A. Crystal Structure and Theoretical Analysis of Green Gold Au30(S-TBu)18 Nanomolecules and Their Relation to Au30S(S-TBu)18. *J. Phys. Chem. C* **2016**, *120* (11), 6256–6261. https://doi.org/10.1021/acs.jpcc.6b00062.

(2) Sakthivel, N. A.; Dass, A. Aromatic Thiolate-Protected Series of Gold Nanomolecules and a Contrary Structural Trend in Size Evolution. *Acc. Chem. Res.* **2018**, *51* (8), 1774–1783. https://doi.org/10.1021/acs.accounts.8b00150.

(3) Crasto, D.; Malola, S.; Brosofsky, G.; Dass, A.; Häkkinen, H. Single Crystal XRD Structure and Theoretical Analysis of the Chiral Au30S(S-t-Bu)18 Cluster. *J. Am. Chem. Soc.* **2014**, *136* (13), 5000–5005. https://doi.org/10.1021/ja412141j.

(4) Zeng, C.; Chen, Y.; Das, A.; Jin, R. Transformation Chemistry of Gold Nanoclusters: From One Stable Size to Another. *J. Phys. Chem. Lett.* **2015**, *6* (15), 2976–2986. https://doi.org/10.1021/acs.jpclett.5b01150.

(5) Angel, L. A.; Majors, L. T.; Dharmaratne, A. C.; Dass, A. Ion Mobility Mass Spectrometry of Au25(SCH2CH2Ph)18 Nanoclusters. *ACS Nano* **2010**, *4* (8), 4691–4700. https://doi.org/10.1021/nn1012447.

(6) Rambukwella, M.; Sakthivel, N. A.; Delcamp, J. H.; Sementa, L.; Fortunelli, A.; Dass, A. Ligand Structure Determines Nanoparticles' Atomic Structure, Metal-Ligand Interface and Properties. *Front. Chem.* **2018**, *6*. https://doi.org/10.3389/fchem.2018.00330.

(7) Nasaruddin, R. R.; Chen, T.; Yan, N.; Xie, J. Roles of Thiolate Ligands in the Synthesis, Properties and Catalytic Application of Gold Nanoclusters. *Coord. Chem. Rev.* **2018**, *368*, 60–79. https://doi.org/10.1016/j.ccr.2018.04.016.

(8) Elahi, N.; Kamali, M.; Baghersad, M. H. Recent Biomedical Applications of Gold Nanoparticles: A Review. *Talanta* **2018**, *184*, 537–556. https://doi.org/10.1016/j.talanta.2018.02.088.

(9) Hillenkamp, F.; Karas, M.; Beavis, R. C.; Chait, B. T. Matrix-Assisted Laser Desorption/Ionization Mass Spectrometry of Biopolymers. *Anal. Chem.* **1991**, *63* (24), 1193A-1203A. https://doi.org/10.1021/ac00024a002.

(10) Kouchi, H.; Kawasaki, H.; Arakawa, R. A New Matrix of MALDI-TOF MS for the Analysis of Thiolate-Protected Gold Clusters. *Anal Methods* **2012**, *4* (11), 3600–3603. https://doi.org/10.1039/C2AY26013A.

(11) Dass, A. Mass Spectrometric Identification of Au68(SR)34 Molecular Gold Nanoclusters with 34-Electron Shell Closing. *J. Am. Chem. Soc.* **2009**, *131* (33), 11666–11667. https://doi.org/10.1021/ja904713f.

(12) Dass, A.; Stevenson, A.; Dubay, G. R.; Tracy, J. B.; Murray, R. W. Nanoparticle MALDI-TOF Mass Spectrometry without Fragmentation: Au25(SCH2CH2Ph)18 and Mixed Monolayer Au25(SCH2CH2Ph)18−x(L)x. *J. Am. Chem. Soc.* **2008**, *130* (18), 5940–5946. https://doi.org/10.1021/ja710323t.

(13) Charles, L. MALDI of Synthetic Polymers with Labile End-Groups. *Mass Spectrom. Rev.* **2014**, *33* (6), 523–543. https://doi.org/10.1002/mas.21403.

(14) Amendola, V.; Meneghetti, M. Size Evaluation of Gold Nanoparticles by UV−vis Spectroscopy. *J. Phys. Chem. C* **2009**, *113* (11), 4277–4285. https://doi.org/10.1021/jp8082425.

(15) Haiss, W.; Thanh, N. T. K.; Aveyard, J.; Fernig, D. G. Determination of Size and Concentration of Gold Nanoparticles from UV−Vis Spectra. *Anal. Chem.* **2007**, *79* (11), 4215–4221. https://doi.org/10.1021/ac0702084.

(16) Sakthivel, N. A.; Jupally, V. R.; Eswaramoorthy, S. K.; Wijesinghe, K. H.; Nimmala, P. R.; Kumara, C.; Rambukwella, M.; Jones, T.; Dass, A. Size Exclusion Chromatography: An Indispensable Tool for the Isolation of Monodisperse Gold Nanomolecules. *Anal. Chem.* **2021**, *93* (8), 3987–3996. https://doi.org/10.1021/acs.analchem.0c04961.